

Supplementary Material

# Seeded-Growth of WS<sub>2</sub> Atomic layers: The Effect on Chemical and Optical Properties

Avinash Patsha, Vered Sheff and Ariel Ismach

Department of Materials Science and Engineering, Tel Aviv University, Ramat Aviv, Tel Aviv, 6997801, Israel

E-mail: [aismach@tauex.tau.ac.il](mailto:aismach@tauex.tau.ac.il)

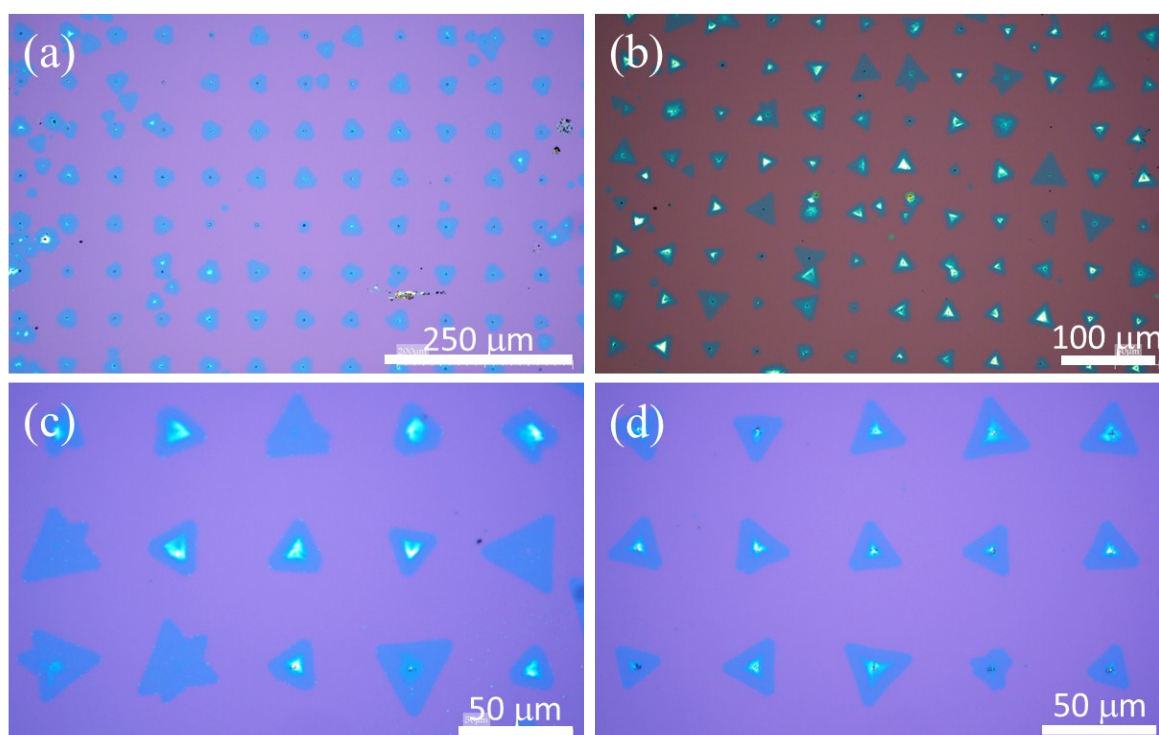


**Figure S1.** Additional optical microscope images showing the vast majority of single-crystal WS<sub>2</sub> domains.

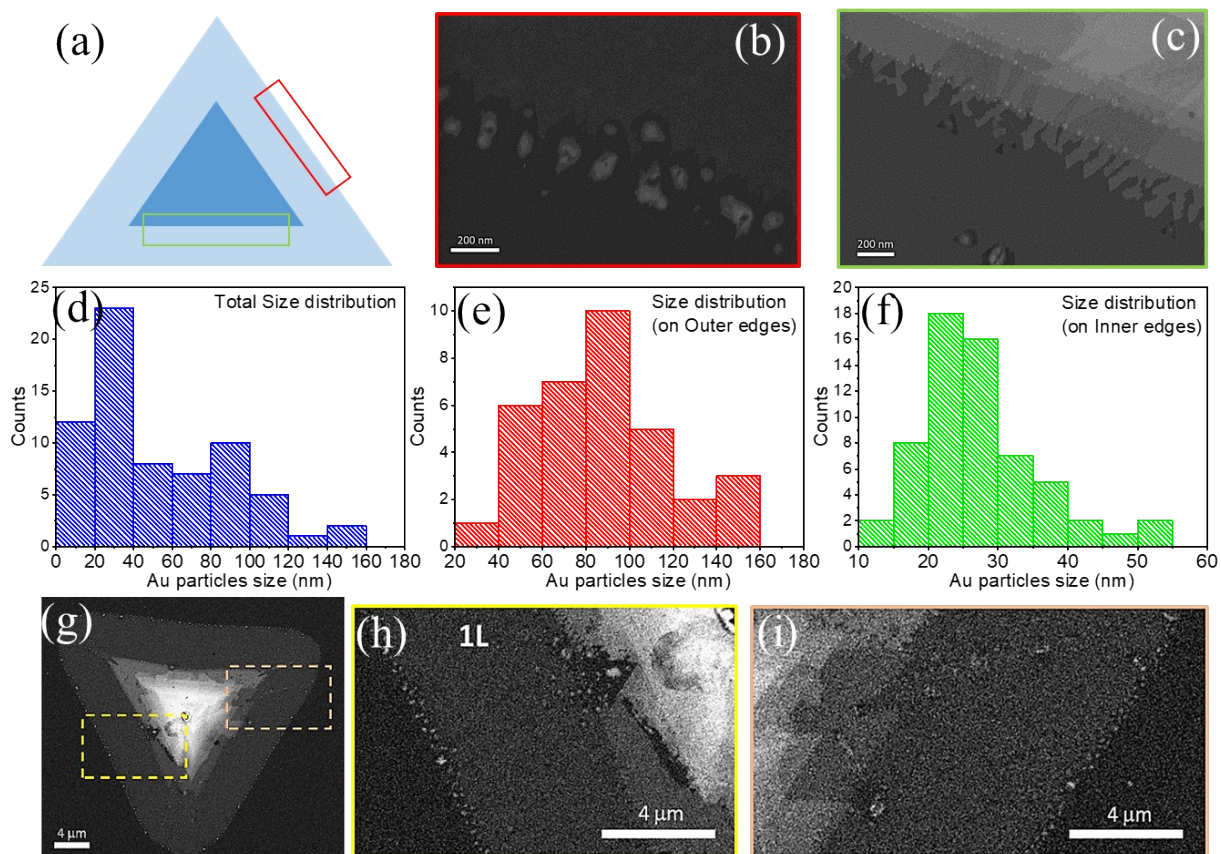
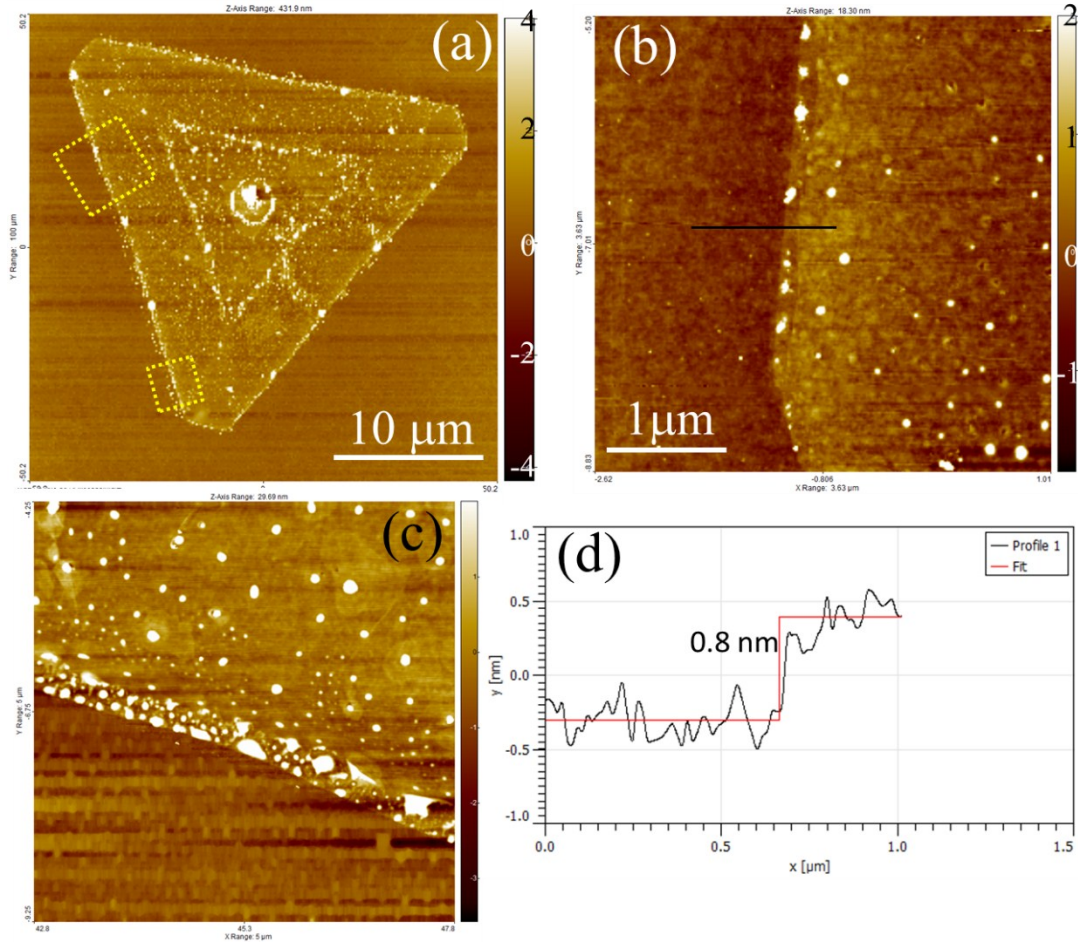


**Figure S2.** The size distributions of Au NPs on Au-seeded WS<sub>2</sub> domains estimated from BSE micrographs. (a) Schematic of a triangular monolayer WS<sub>2</sub> domain (light blue) with ad-layers at the center (dark blue). (b) – (c) BSE SEM images taken from the outer edges (red) and from the interface between the ad-layers and the monolayer region (green). (d) The total size distribution of NPs from all the regions of WS<sub>2</sub> domains, (e) NPs from outer edges of the monolayer WS<sub>2</sub> domain, and (f) inner edges of the ad-layer WS<sub>2</sub> triangles. (g)-(i) BSE images from a whole domain, and enlarged areas showing a NP wide size distribution on the sides of the monolayer region.



**Figures S3.** AFM Characterization. (a) Topography map of a truncated triangular WS<sub>2</sub> domain showing the dispersion of NPs on it. (b) and (c) High resolution maps of the edges of the domain in (a), corresponding to the two dotted squares in (a), the small, a  $3 \times 3 \mu\text{m}^2$  area is shown in (b), and the  $5 \times 5 \mu\text{m}^2$  image is shown in (c). (d) The line profile, black line in (b), shows a  $\sim 0.8$  nm thick layer corresponding to a single layer.

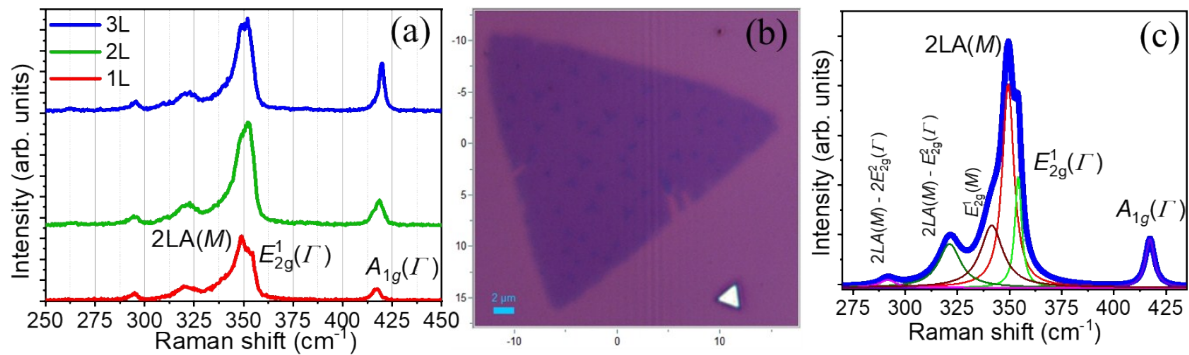


**Figure S4.** (a) The comparison of layer dependent Raman spectra recorded from pristine WS<sub>2</sub> atomic layers grown without any Au seeds. (b) Pristine triangular WS<sub>2</sub> domain grown without Au-seeds and corresponding Raman spectra (c).

The Raman spectra of 1L, 2L, and 3L WS<sub>2</sub> were recorded from WS<sub>2</sub> atomic layers grown without Au seeds (Figure S2), for the study of layer dependent characteristics. As the layer number increases from 1L to 3L, the Raman intensity ratio  $I(2LA(M)) / I(A_{1g})$  decreased from 4.2 for 1L to 1.1 for 3L. In addition, Raman intensity of 2LA(M) mode is dominated over  $E^1_{2g}(I)$  mode for 1L as compared to 2L and 3L.

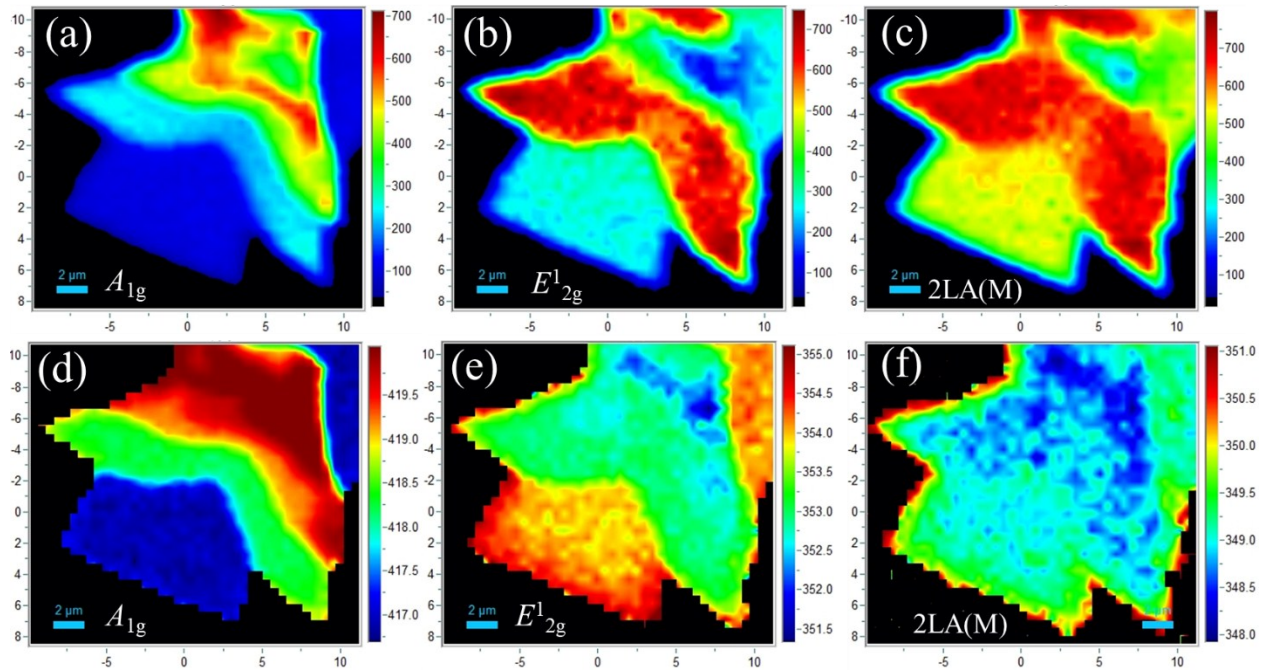


**Figure S5.** The Raman maps of (a-c) peak intensity, and (d-f) peak position of  $A_{1g}$ ,  $E^1_{2g}$ , 2LA(M) modes recorded from pristine WS<sub>2</sub> atomic layers grown without Au seeds, respectively.

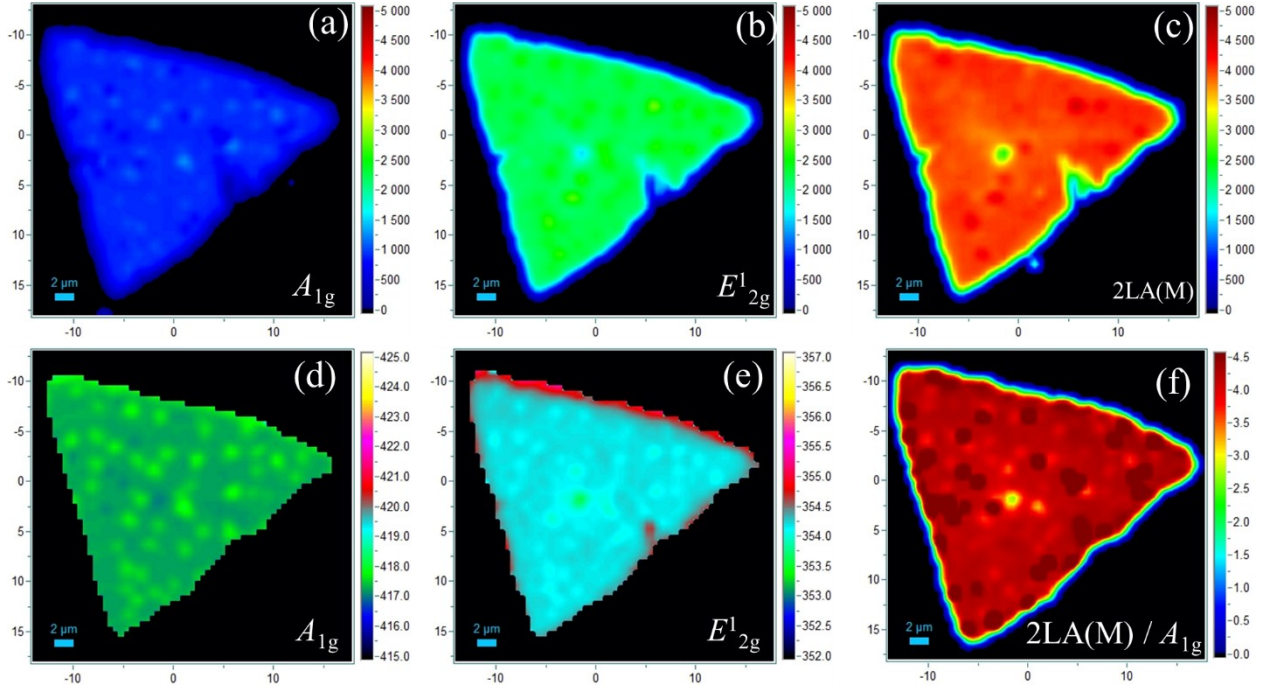


**Figure S6.** The Raman maps of (a-c) peak intensity, and (d-f) peak position of  $A_{1g}$ ,  $E^1_{2g}$ ,  $2LA(M)$  modes recorded from pristine monolayer triangular  $WS_2$  domain grown without Au seeds, respectively.

The Raman spectral maps of  $A_{1g}$ ,  $E^1_{2g}$ ,  $2LA(M)$  modes were recorded from pristine  $WS_2$  atomic layers grown without Au seeds (Figure S4, S5). As the layer number increases, the peak intensity of  $A_{1g}$  mode,  $I(A_{1g})$  increased by a factor of 3 (Figure S4a). Whereas,  $I(E^1_{2g})$  and  $I(2LA(M))$  modes are enhanced for 3L as compared to 1L (Figure S3b,c). The Raman peak position map of  $A_{1g}$  mode show clear contrast among the layer numbers. As the layer number increases from 1L to 3L,  $A_{1g}$  mode is shifted from  $417.0$  to  $419.5 \text{ cm}^{-1}$  (Figure S4d). While the contrast of peak position map of  $E^1_{2g}$  mode show very minute shift of  $1.5 \text{ cm}^{-1}$  among 1L and 3L. The peak position map of the  $2LA(M)$  mode hardly show any contrast among all the layers. The sharp features at edges in peak position maps are due to the truncation of mapping grid selected for the Raman mappings and due to curve fitting process of the data.

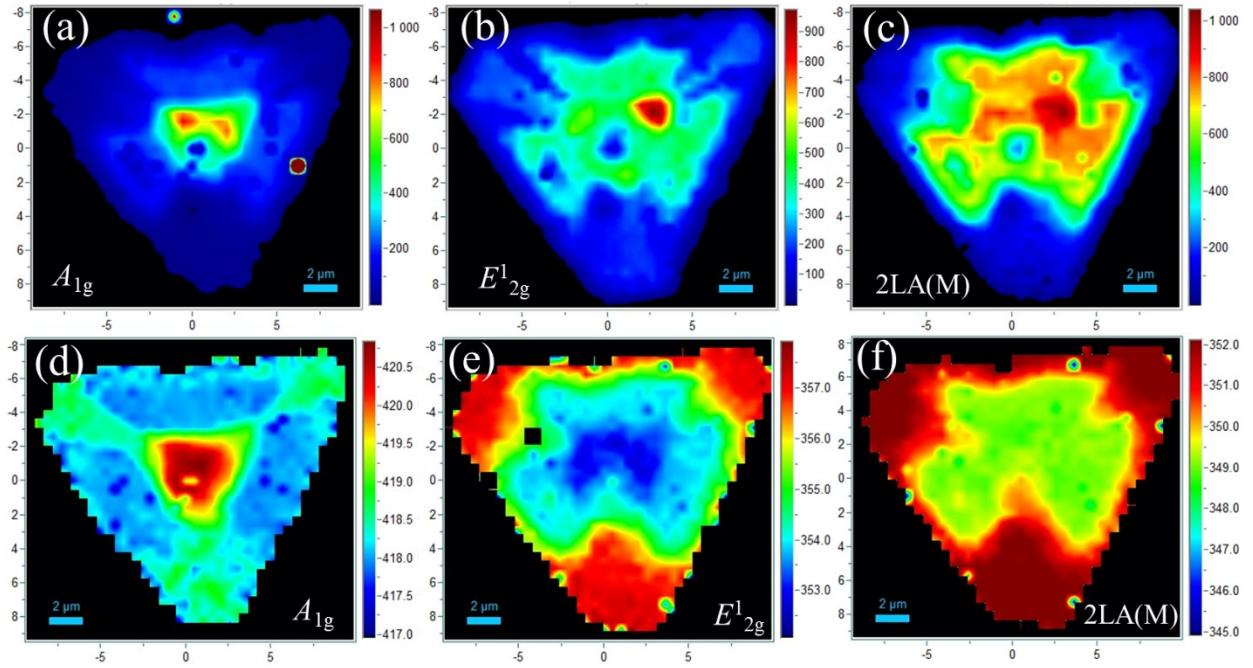


**Figure S7.** The Raman maps of (a-c) peak intensity, and (d-f) peak position of  $A_{1g}$ ,  $E^1_{2g}$ ,  $2LA(M)$  modes recorded from Au-seeded  $WS_2$  domain, respectively.

The Raman spectral maps of  $A_{1g}$ ,  $E^1_{2g}$ ,  $2LA(M)$  modes were recorded from  $WS_2$  atomic layers grown with Au seeds (Figure S6). The distribution of  $I(A_{1g})$  is found to be lowest all over the triangle except at the center where Au seeds are present (Figure S6a). In addition, very little enhancement in the  $I(A_{1g})$  is observed at the 3 sides of the triangle as compared to vertices. The contrast of  $I(E^1_{2g})$  shows a peculiar contrast among vertices and sides (Figure S6b). The peak position map of  $A_{1g}$  mode showed highest shift ( $\sim 421$ ) at the center as compared to that of three sides of the triangle ( $\sim 418$ ).

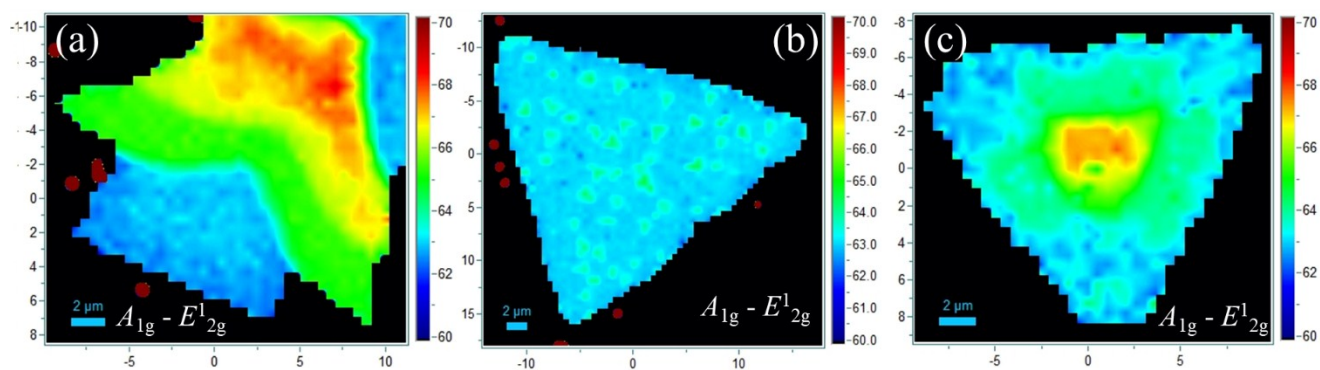


**Figure S8.** The Raman maps of peak position difference of  $A_{1g}$ ,  $E_{2g}^1$  modes recorded from (a) pristine  $WS_2$  layers, (b) pristine  $WS_2$  triangle, and (c) Au-seeded  $WS_2$  domain, respectively.

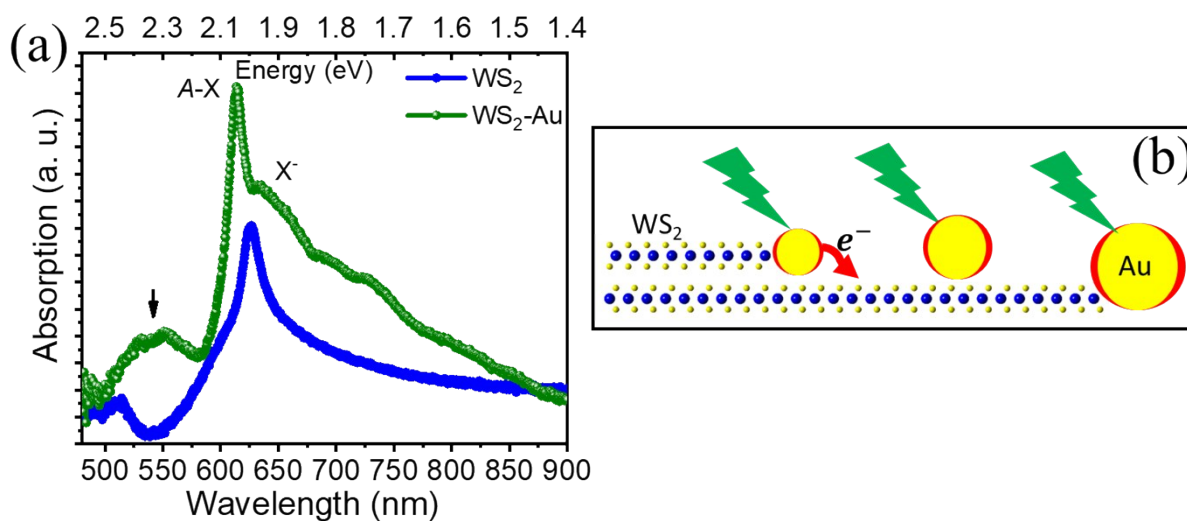


**Figure S9.** (a) The micro-absorption spectra collected on pristine  $WS_2$  triangle (blue in color) and on single Au-seeded  $WS_2$  domain (green in color). The arrow mark shows the broad SPR absorption corresponding to Au NPs. (b) Schematic of the Au NP arrangement on the  $WS_2$  domains showing the different NP sizes and the two possible plasmonic interaction with the  $WS_2$  (hot-electron transfer and LSPR).

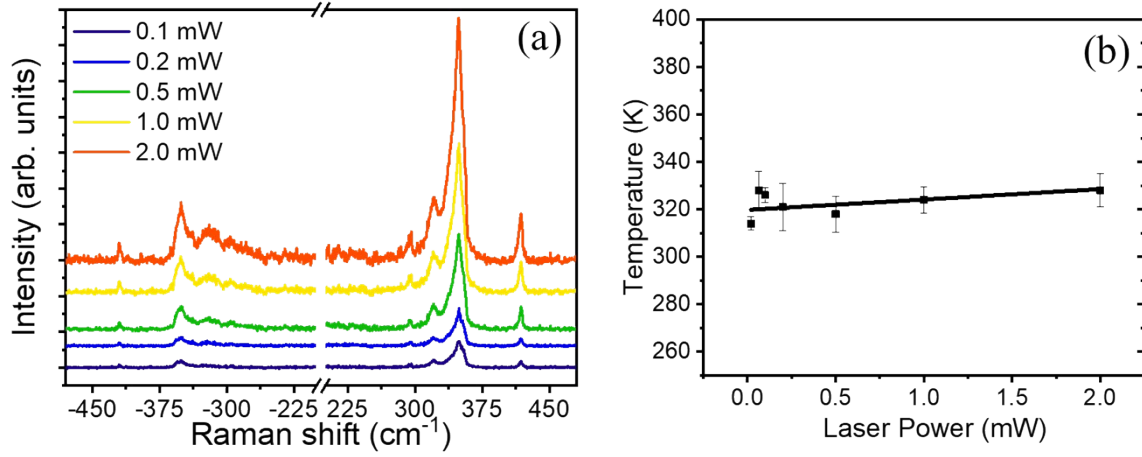


**Figure S10.** (a) The Stokes and Anti-stokes Raman spectra of Au-seeded WS<sub>2</sub> domains, recorded at different laser powers on the sample and, (b) the corresponding plot of temperature Vs laser power.

The local temperatures generated by different laser powers on Au-seeded WS<sub>2</sub> domain are estimated by recording the stokes- and anti-stokes Raman spectra using a set of notch filters for 532 nm. Note that the values of laser powers used for these measurements are slightly different, though in same order, from that of the PL measurements due to the difference in Rayleigh rejection filter sets, 532 nm notch and edge filters, respectively. No significant change in the peak positions of the Raman modes are observed for all the laser powers used (Figure S9(a)), indicating the negligible effect of temperature generated by the corresponding laser powers. The local temperatures are estimated by extracting the ratio of integral intensities of stokes- and anti-stokes Raman mode  $\sim 350$  cm<sup>-1</sup> using

$$I_S / I_{AS} = \exp(\hbar \omega / K_B T),$$

Where,  $I_S$ ,  $I_{AS}$  are the integral intensities of stokes and anti-stokes components of the corresponding Raman mode and,  $\omega$  being vibrational frequency,  $K_B$  being Boltzmann constant, and  $T$  being temperature. The maximum variation in temperature while changing the laser powers, is around  $\pm 10$  K (Figure S9(b)).

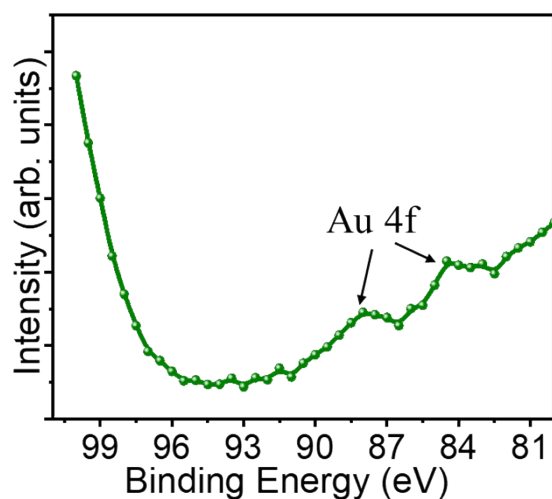


**Figure S11.** The XPS spectra of Au 4f from Au seeded WS<sub>2</sub> domains.

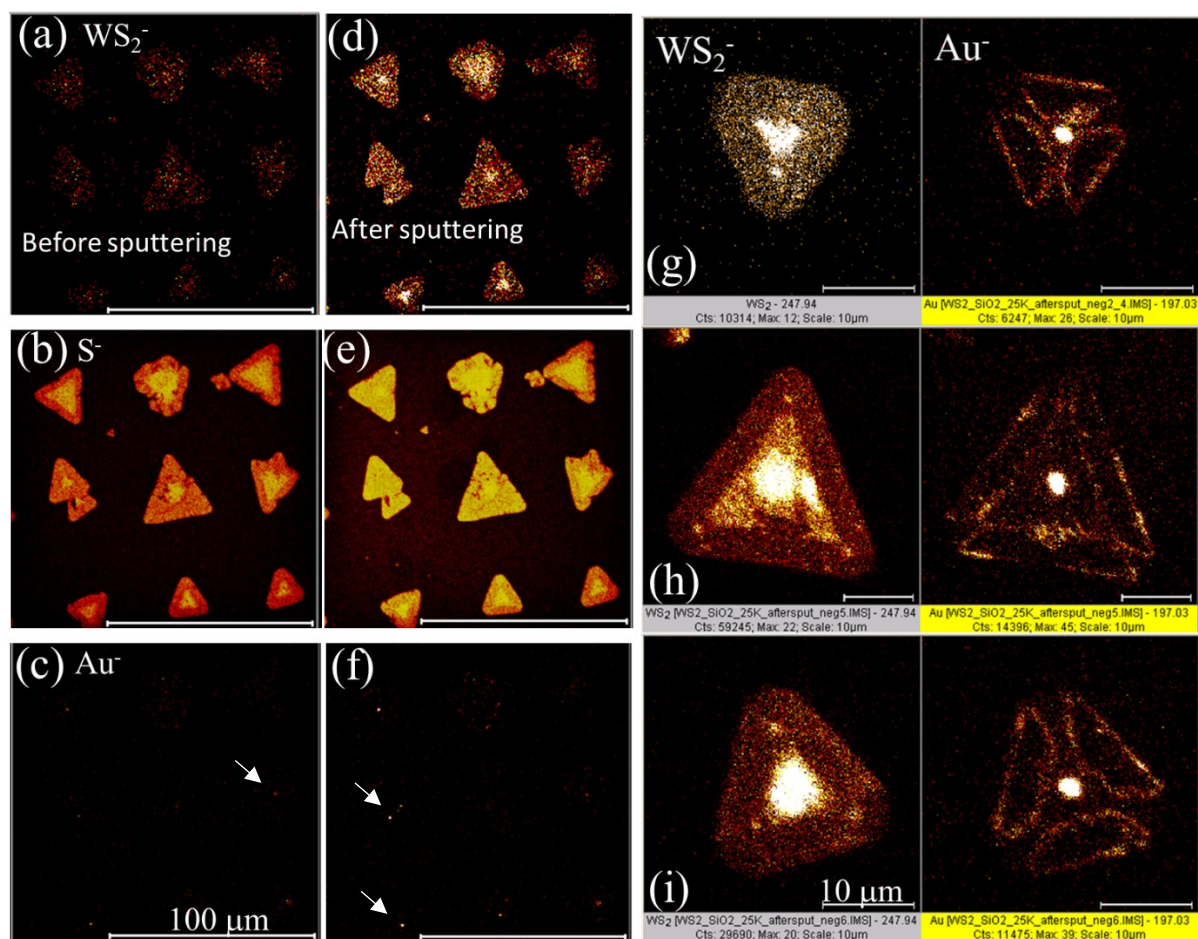


**Figure S12. Further TOF-SIMS Characterization:** (a)-(c) Mappings before a mild sputtering to clean the surface from contaminants. (d)-(f) Same areas after the sputtering. (g)-(i) High magnification TOF-SIMS mappings for WS<sub>2</sub><sup>-</sup> (left side) and Au<sup>-</sup> ions (right side) of Au seeded WS<sub>2</sub> domains. The scale bar is 10 μm.

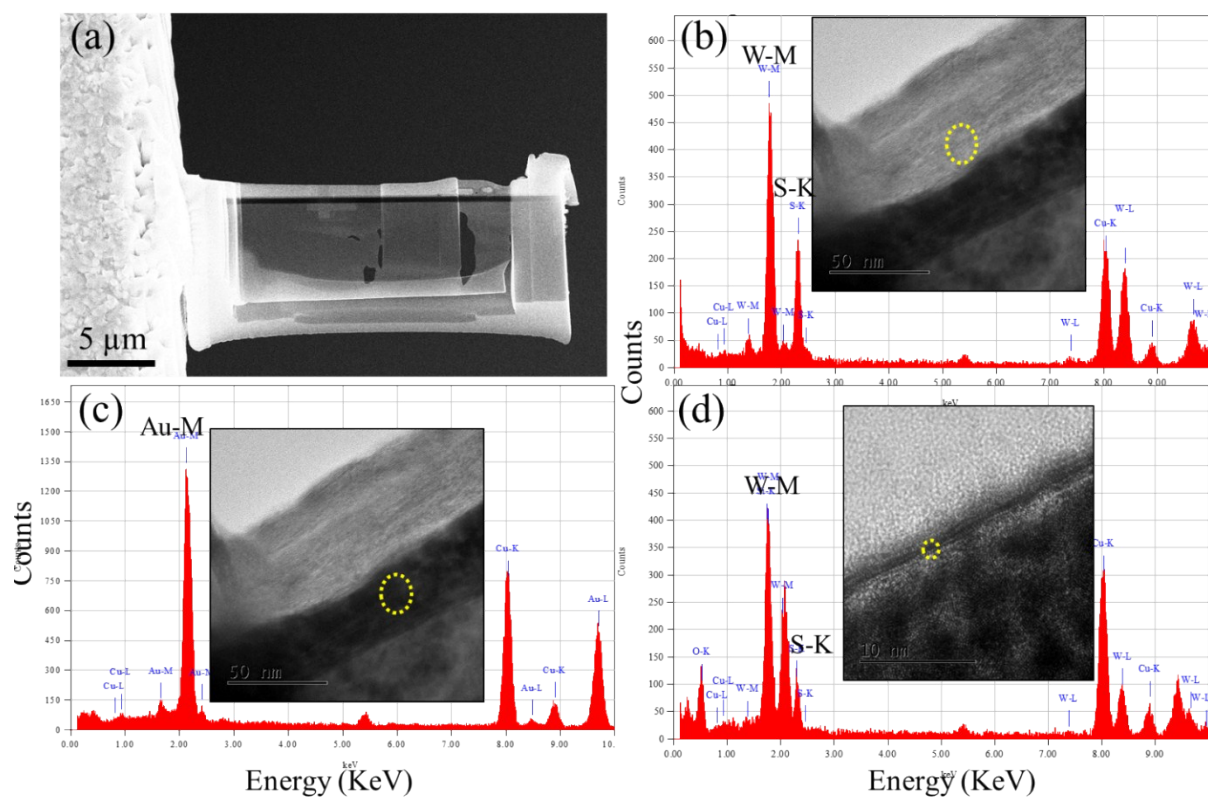


**Figure S13.** (a) The FESEM micrograph of the cross-sectional TEM lamella. (b)-(d) The EDS spectra recorded at different locations of the specimen as shown in the insets. The dotted circles denote the regions of spectra collected.